

# MEMS Scanners for Display and Imaging Applications

Hakan Urey

Electrical Engineering Department and Optical Microsystems Laboratory  
Koç University, Istanbul-TURKEY

## ABSTRACT

Dynamic display and imaging applications demand high performance scanners, which has high frequency (exceeding 10KHz), large scan-angle-mirror-size product ( $>\pm 10\text{deg}\cdot\text{mm}$ ), good optical surface quality ( $<\lambda/20$  static and dynamic flatness), high sensitivity position sensors, and high-torque actuators that are compact and low power. This paper discusses the resolution and other optical performance requirements for diffraction-limited and non-diffraction-limited light sources in a scanning system. A set of analytical formulas is presented for calculating the torsion and other four fundamental oscillation mode vibration frequencies. The formulas include the effects of material anisotropy in orthotropic materials, such as Silicon and effective mass and inertia of the flexures. The validity range of formulas are extended by introducing a correction factor based on flexure width and flexure length ratios. The formulas are very efficient for performance trades and optimization. For scanner actuation, we present two compact scanner actuation mechanisms: out-of-plane comb actuator and novel two-coil electromagnetic actuator.

**Keywords:** scanners, modeling, torsion, actuator, electrostatic, electromagnetic

## 1. INTRODUCTION

Integration of scanners and diode light sources (e.g. laser diodes, LEDs) provide a powerful combination for microdisplay and imaging applications. This is exemplified by the commercial applications such as laser printers, barcode readers, and by wearable microdisplay systems that use MEMS scanners. Dynamic display and imaging applications demand high performance scanners, which has high frequency (exceeding 10KHz), large scan-angle-mirror-size product ( $>\pm 10\text{deg}\cdot\text{mm}$ ), good optical surface quality ( $<\lambda/20$  static and dynamic flatness), high sensitivity position sensors, and high-torque actuators that are compact and low power.

One of the system design goals is to obtain good separation of vibration modes with respect to torsion while providing a fast and compact actuator to meet the actuation force requirements at reasonable voltage and power levels is an important system design challenge. In this paper, we first discuss the resolution and other optical performance requirements for scanning systems that use diffraction-limited and non-diffraction-limited light sources. Section 4 discusses resonant MEMS scanner mechanical design and provides a set of analytical formulas that are useful for performance trades and optimization. In section 5, we present two compact scanner actuation mechanisms: out-of-plane comb actuator and moving coil electromagnetic actuator.

## 2. RETINAL SCANNING DISPLAY OPERATION

Retinal Scanning Display (RSD) is an exemplary system where MEMS scanners play a key role<sup>1</sup>. RSD operate by scanning a light beam onto the viewer's retina in a 2-D raster format. As illustrated in Figure 1, optics for the RSD includes an intermediate image plane between the scanner and the exit pupil of the display and typically produces a small exit pupil. This limitation can be traced to the optical invariant or the Lagrange invariant and can be removed using an exit pupil expander (EPE) at the intermediate image plane. The EPE is essentially a forward-scattering diffuser screen that increases the exit pupil size from the typical 1-2mm to 15mm or larger. The EPE can be implemented using a periodic 2-D diffraction grating<sup>2</sup> or using one or two cascaded microlenses<sup>3</sup> that creates replicas of the 1-2mm pupil across a much larger exit pupil). The large exit pupil allows the user's eye and head to move relative to the display over a large range without losing the image.

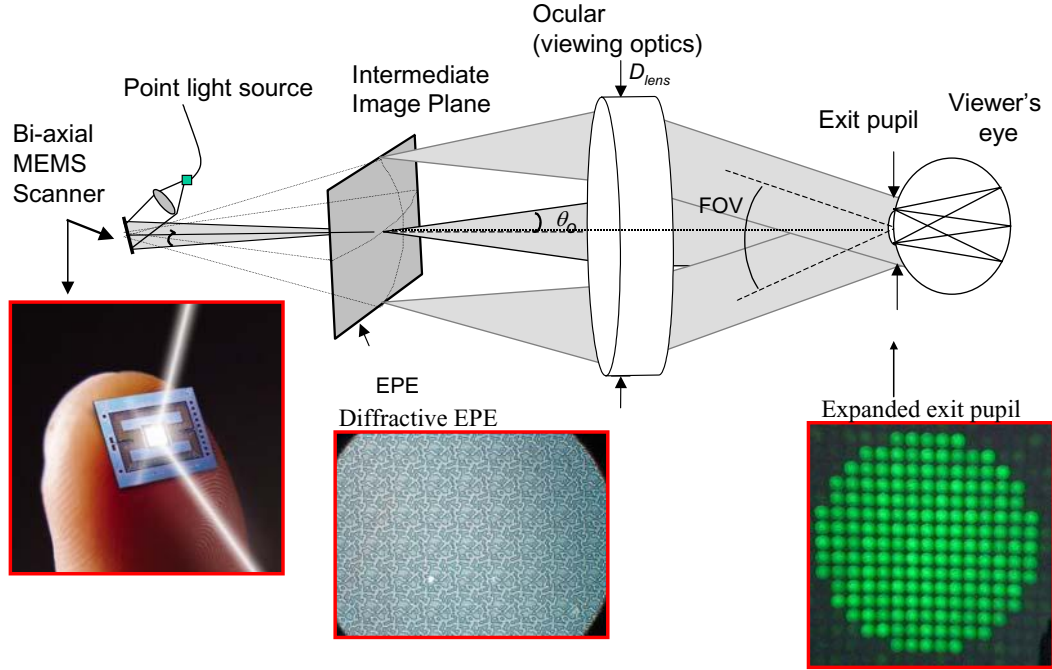


Figure 1: Scanned beam display optics including exit pupil expander (EPE) at the intermediate image plane. Expanded exit pupil is made up of an array of diffraction orders due to periodic structure of the 2-D diffraction grating illustrated in the figure.

### 3. RESOLUTION AND OPTICAL REQUIREMENTS

Mirror size, scan angle, and scan frequency requirements of the scanner is derived from the optical resolution requirements of the display or imaging system. Light sources play a key role. We'll treat diffraction-limited and non-diffraction-limited sources separately and drive a resolution equation based on scan mirror size and scan angle. Paraxial approximation (i.e., small angle assumption,  $\theta = \sin \theta = \tan \theta$ ) is assumed throughout the analysis.

**Diffraction-Limited Sources:** Diffraction limited laser beams or the beam exiting a single-mode optical fiber have a Gaussian profile. For systems that use a laser or fiber as the illumination source, the PSF is primarily determined by the clipping ratio of the beam at the system aperture. The beam truncation ratio,  $T$ , can be defined as the ratio of feed beam  $1/e^2$  intensity diameter (FWE2) at the system exit pupil to the exit pupil diameter (ratio of beam diameter to the mirror clear aperture diameter if the scanner is the limiting aperture). The PSF size may be defined as the full width of the diffracted beam at its half power points  $s_{FWHM}$ :

$$s_{FWHM} = K_T \lambda f_{\#} \quad (1)$$

where  $K_T$  is a constant that is a function of  $T$  and is given by<sup>4</sup>

$$K_T = 1.037 - \frac{0.057}{T} + \frac{0.156}{T^2}, \quad T > 0.4 \text{ (Clipped Gaussian)} \quad (2)$$

$$K_T = \frac{0.75}{T}, \quad T < 0.5 \text{ (Gaussian)} \quad (3)$$

If the scanner serves as the aperture stop of the system, then the number of resolvable spots may be written in terms of the full optical scan angle  $\theta_{opt}$ , the mechanical zero-to-peak angle  $\theta_{mech}$ , and the mirror diameter  $D$  according to

$$N = \frac{K_{sys} \theta_{opt} D}{K_T \lambda} = \frac{4K_{sys} \theta_{mech} D}{K_T \lambda} \quad (4)$$

where  $K_{sys}$  is in the order of unity and includes the effects of many system design parameters<sup>1</sup>. The number of resolvable spots for a coherent focusing geometry system that is diffraction limited thus depends on the  $\theta D$ -product of the scanner, one of the key performance metrics for optical scanners. Note that, for center-pivot scanners,  $\theta D$  also corresponds to the full-excursion motion of the edge of the scanner.

Table 1 shows the  $\theta D$  requirements for high-performance RSDs. For instance, an SVGA scanning display system can be implemented using a 1mm scanner that scans  $\pm 9.7$ deg mechanically. This system would indeed produce very high display contrast modulation for high spatial frequency features (i.e. high display MTF). One can reduce the  $\theta D$  requirements from the values given in the table by increasing the spot overlap between adjacent pixels, at the expense of contrast modulation and edge sharpness in the displayed images and video.

**Table 1**  $\theta D$ -product and scanner frequency requirements for various display formats (see Ref. [1] for assumptions on system design parameters)

Display Format	QVGA	VGA	SVGA	XGA	SXGA	UXGA	HDTV
$N_h$ - Horizontal resolution	320	640	800	1024	1280	1600	1920
$N_v$ - Vertical resolution	240	480	600	768	1024	1200	1080
$\theta_{mech} \cdot D$ (deg.mm)	3.9	7.8	9.7	12.4	15.6	19.4	23.3
$f_s$ - Horizontal scanner freq. (Hz)	8000	16000	20000	25600	34133	40000	36000

**Non-Diffraction-Limited Sources:** Above resolution equation is valid when a diffraction-limited source is used. When an extended, non-single-mode source such as an edge-emitting LED is used in the system, the pixel size on the intermediate image plane follows from the magnification of the collection optics:<sup>5</sup>

$$s_{pixel} = s_{emitter} \frac{NA_{collect}}{NA_{scan}} \quad (5)$$

Where  $s_{emitter}$  is the effective emitter size and  $NA_{collect}$  is the collection NA of the optics. Typically, the MEMS mirror is the effective limiting aperture in these systems, so that  $NA_{scan}$  is given by  $D/2z$ , where  $z$  is the distance from scanner to the intermediate image plane. When extended sources are used, the number of resolvable pixels can be expressed as

$$N = \frac{L}{s_{pixel}} = \frac{2\theta_{mech} D}{s_{emitter} NA_{collect}} \quad (6)$$

This important relation ties together the parameters of the MEMS scanner with the light collection properties of the system. The denominator effectively determines the amount of power that can be put into a single pixel from a source of given radiance.

Dynamic mirror distortion due to large acceleration forces during scanning is an important limitation. Scanner needs to be thick enough to maintain a flatness that is better than  $\lambda/20$  both statically and dynamically. There are several additional scanner performance parameters that impact the image quality. For instance, line-to-line jitter and frame-to-frame jitter depend on how accurately the scan position and the frequency can be synchronized with the data clock and the vertical scanner. The total jitter in the system should be at sub-pixel levels. For a high-quality SVGA system, if we assume a maximum of 1/8 pixel off-axis motion for the horizontal scanner, the jitter in the system including the electronics, the position sensor, and the mechanical scanner should not exceed 3-4 nsec. This imposes constraints on the non-linearity of the vertical scan and the determination of mirror position and the scanner frequency. Typically, the

vertical scan nonlinearity should be less than 1%, or in some cases even 0.1% across the vertical scan line and the horizontal scanner position measurement accuracy needs to be within 0.025% (1/4000).<sup>6</sup>

#### 4. SCANNER MECHANICAL DESIGN

The following steps can be followed for the scanner design:

- Choose the mirror size and scan angle based on system architecture and  $\theta D$ -product requirements
- Choose mirror thickness and geometry to meet dynamic mirror flatness requirements
- Design flexures to meet torsion frequency, stress, and vibration mode separation requirements
- Design actuator to meet torque requirements
- Design position sensors
- Design process to minimize die size and packaged device cost requirements

First step is addressed in the previous section. For rectangular block mirrors, mirror thickness requirement can be calculated using 1<sup>st</sup> order dynamic distortion equations<sup>7</sup>, for more complex geometries FEM should be used. High-resolution and high-frequency scanning requires scanners that are large and thick. Surface micromachined MEMS scanners do not meet the static and dynamic mirror flatness requirements at high frequencies. The required force and torque in such scanners are also large.

In the remainder of this section, we focus on the 3<sup>rd</sup> step of this procedure and present formulas and FEM results for estimating torsion and other vibration mode frequencies, and torsional stress to facilitate flexure mechanical design and optimization.

##### 4.1. Scanner Natural Vibration Modes

Basic one-axis torsional scanner geometry and the first five fundamental vibration modes are illustrated in Figure 2. Two-axis scanners can be obtained by cascading two scan frames, one inside the other. Mirror vibration frequency requirements determine the flexure beam dimensions that suspend the mirror.<sup>7</sup> Thus, predicting the frequencies for the torsion and other fundamental vibration modes is critical. If torsion is the desired mode, other modes are often undesired and should be well separated from the torsional mode frequency and its harmonics. As an example, in some applications, torsion and out-of-plane rocking mode should have a certain mode separation for simultaneous excitation.<sup>8</sup> FEM simulations are time consuming and engineering of the vibration mode frequencies for the optimal design is difficult without having good analytical models for fast calculations.

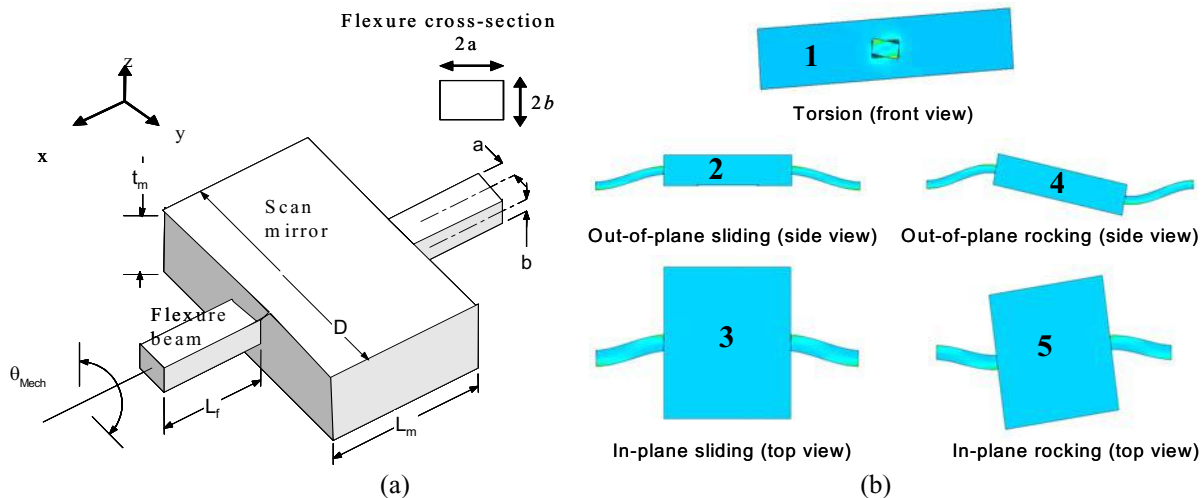


Figure 2 (a) Torsional resonant scan mirror suspended with two flexure beams that are fixed at the ends, figure inset shows flexure rectangular cross-section and coordinate axis; (b) five fundamental vibration modes for the torsional scanner, which are rotation around x-axis (torsional), translation in z-axis (out-of-plane translation), translation in y-axis (in-plane sliding), rotation around y-axis (out-of-plane rocking), and rotation around z-axis (in-plane rocking).

One can calculate the natural frequencies of each vibration mode by using appropriate displacement or rotation angle variable, spring constant, and effective mass or effective mass moment of inertia terms. As an example, the natural frequency for the vibration mode along y-axis (in-plane sliding) with angular frequency ( $\omega=2\pi f$ ) can be calculated by:<sup>9</sup>

$$\frac{d^2y}{dt^2} + \omega^2 y = 0 \quad (7)$$

$$\omega = 2\pi f = \sqrt{K_s / M_{eff}} \quad (8)$$

where  $K_s$  is the spring constant for the mode and  $M_{eff}$  is the effective mass of the scan mirror for the particular vibration mode. Throughout our analysis, the mirror plate is assumed rigid and flexures are assumed fixed on either end. In addition, damping is ignored in Eq. (7) because of the typically negligible effect on the natural frequency for underdamped systems.

Table 2 summarizes the spring constant, effective inertia including the flexure-inertia terms for 5 fundamental modes. The formulas for the spring constants are consistent with values given elsewhere in the literature<sup>10-12</sup>. Table 3 gives mirror inertia for different mirror shapes. The natural frequency of a mode can be calculated using (8).

The torsion mode solution given in Table 2, the shape factor GK-product formula works very well even for extreme flexure width to thickness ratios such as 0.05 or 20. The coefficient  $\mu = \sqrt{G_{xz} / G_{xy}}$ , defined for torsion of orthotropic materials such as Silicon, is due to material anisotropy and is equal to 1 for isotropic materials. Even though single-crystal Silicon is anisotropic, some of the MEMS literature use  $\mu=1$  in the above expressions for computing torsional stiffness for Silicon<sup>10-14</sup>. Using the correct  $\mu=1.248$  for  $\langle 100 \rangle$  Silicon in our new formula improves the accuracy of the torsional stiffness computation by as much as 20 % in some cases. This is one of the important results of our analytical study.

#### 4.2. Parametric Study of Flexure Dimensions

Using three flexure dimensions and imposing a constraint on the torsion frequency, we can define two dimensionless flexure parameters  $k$  and  $n$ . The  $k$  parameter is equal to ratio of larger of the two sides of the rectangular cross-section to smaller of the two sides (i.e.,  $k=a/b$  for  $a>b$  and  $k=b/a$  for  $b>a$ ). The  $n$  parameter is the ratio of the beam length  $L_f$  to the larger of the two sides of the rectangular beam cross-section. Assuming  $a>b$ , for a given  $(k,n)$  pair and torsional frequency  $f$  and assuming rectangular block mirror, the flexure dimensions can be calculated as:

$$a = \left[ \frac{4\pi^2 f^2 k^3 n J_{m,xx}}{G_{xy} (5.33 - 3.36 \frac{1}{k\mu} [1 - \frac{1}{12(k\mu)^4}])} \right]^{\frac{1}{3}} \quad (9)$$

$$b = \frac{a}{k}, \quad a>b \text{ assumed} \quad (10)$$

$$L_f = 2na \quad (11)$$

The aim of the parametric study using dimensionless parameters is to make the results of error analysis applicable to other scanner designs that have the same flexure ratio parameters  $(k,n)$  but different mirror dimensions and torsion frequencies. An error is defined using analytical and FEM frequency predictions:

$$\% \text{ error} = 100 \left[ \frac{f_{fem} - f_a}{f_a} \right] \quad (12)$$

Table 2: Natural frequency for five fundamental oscillation modes for torsional scanners

	Effective Mass ( $M$ ) / Mass Moment of Inertia ( $J_{eff}$ )	Spring Constant, $K_s$
1. Torsion	$J_{eff} = J_{m,xx} + (2/3)J_{f,xx}$ $J_{f,xx} = \frac{1}{3}M_f(a^2 + b^2)$ $M_f = 4abL_f$	$K_s = \frac{2GK}{L_f}$ ; $\mu = \sqrt{G_{xz}/G_{xy}}$ For $a > b$ use below; for $b > a$ , interchange $a$ with $b$ and $G_{xy}$ with $G_{xz}$ $GK \approx (ab^3G_{xy}) \left( 5.33 - 3.36 \frac{b}{a} \frac{1}{\mu} \left( 1 - \frac{b^4}{12a^4\mu^4} \right) \right)$
2. Out-of-plane Sliding	$M_{eff} = M_m + \frac{26}{35}M_f$	$K_s = \frac{24E_x I_{yy}}{L_f^3}$ ; $I_{yy} = \frac{4}{3}ab^3$
3. In-plane Sliding	$M_{eff} = M_m + \frac{26}{35}M_f$	$K_s = \frac{24E_x I_{zz}}{L_f^3}$ ; $I_{zz} = \frac{4}{3}a^3b$
4. Out-of-plane Rocking	$J_{eff} = J_{m,yy} + 2J_f$ $J_f = M_f(0.0095L_f^2$ $+ 0.052L_fL_m + 0.0929L_m^2)$	$K_s = \frac{E_x I_{yy} \left( 2 + 6 \left( 1 + \frac{L_m}{L_f} \right)^2 \right)}{L_f}$
5. In-plane Rocking	$J_{eff} = J_{m,zz} + 2J_f$	$K_s = \frac{E_x I_{zz} \left( 2 + 6 \left( 1 + \frac{L_m}{L_f} \right)^2 \right)}{L_f}$

Table 3: Mass and mass moment of inertia for different mirror ( $M_m$  is the mass of the mirror and  $M_f$  is the mass of one flexure) shapes.

	$M_m$	$J_{m,xx}$	$J_{m,yy}$	$J_{m,zz}$
Rectangular Mirror	$\rho L_m D t_m$	$\frac{M_{mirr}}{12} (D^2 + t_m^2)$	$\frac{M_{mirr}}{12} (L_m^2 + t_m^2)$	$\frac{M_{mirr}}{12} (D^2 + L_m^2)$
Elliptical Mirror	$\frac{\pi}{4} \rho L_m D t_m$	$\frac{M_{mirr}}{12} \left( \frac{3}{4} D^2 + t_m^2 \right)$	$\frac{M_{mirr}}{12} \left( \frac{3}{4} L_m^2 + t_m^2 \right)$	$\frac{M_{mirr}}{16} (D^2 + L_m^2)$
Circular Mirror	$\frac{\pi}{4} \rho D^2 t_m$	$\frac{M_{mirr}}{12} \left( \frac{3}{4} D^2 + t_m^2 \right)$	$\frac{M_{mirr}}{12} \left( \frac{3}{4} D^2 + t_m^2 \right)$	$\frac{M_{mirr}}{8} (D^2)$

Figure 3 summarizes the results of our parametric study, comparing our analytical results with FEM simulations. There are several interesting observations that can be made using the graphs:

Torsion frequency predictions are always within 10% even for wide and short flexures (large  $k$ , small  $n$ ) and within 3% for  $n > 4$ . We separately tested the contribution of the flexure inertia term and it is not negligible especially for large values of  $n$ .

Formulas predict the other 4 vibration mode frequencies to within ~10% for  $n > 6$ . Including the effects of flexure effective mass and flexure effective mass moment of inertia become particularly important for long flexures ( $n > 6$ ). Error

for non-torsion modes is always negative (i.e., formulas over-predict the vibration frequencies). Our model includes constraints on the shear deformations within the suspension and on the deformation of the mirror. Neglecting these deformations causes an over prediction of the stiffness, i.e. the actual spring constant and the frequency are lower than

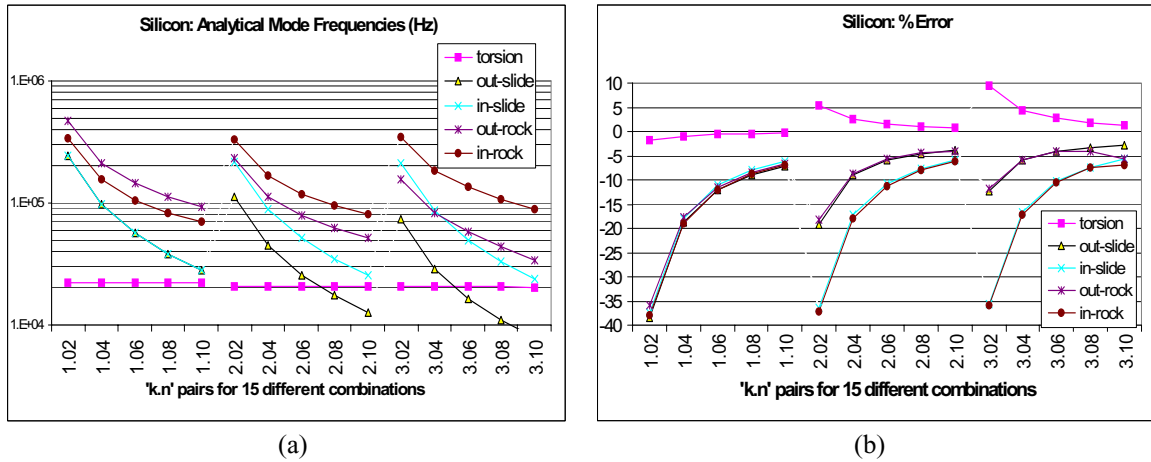


Figure 3: Mode frequency calculations using analytical formulas and percentage error compared to FEM for 15 different microscanner designs (illustrated as  $k.n$  pairs). All microscanners have approximately 20KHz torsion frequency but different flexure dimensions as determined by  $(k,n)$  pairs. Horizontal axes shows  $k.n$  values (e.g. 2.04 means  $k=2, n=4$ ).

the formula predictions. The effect of shear deformations (ignored in Euler-Bernoulli beam theory) becomes particularly significant for small flexure length ratios  $n$ .

Note that the percentage errors corresponding to translation and rocking modes are very similar for both in-plane and out-of-plane modes. This is expected due to symmetries in geometry.

The predictions are valid for  $a > b$  ( $k > 1$ ). If  $b > a$  ( $0 < k < 1$ ), the error results in Figure 3 can still be used. For torsion mode, the errors in either case are about the same. For sliding and rocking modes, the error predictions for in-plane mode and out-of-planes modes should be interchanged.

#### 4.3. Discussion on Vibration Mode Formulas

Tables 2 and 3 give spring constant and inertia terms corresponding to the five fundamental oscillation modes for flexure-mounted scanner designs. Our formulas can handle orthotropic material properties and include effects of flexure beam inertia. Using beam-width-ratio parameter and beam-length-ratio parameter for a scanner design, a correction factor based on error charts in Figure 3 can be added to the analytical formulas to improve the accuracy of the predictions. Using the correction factors, analytical formulas become accurate to within a few percent of FEM predictions in all cases for a broad range of flexure dimensions, including ranges where assumptions underlying Euler-Bernoulli beam theory do not hold.

#### 4.4. Material Stress due to Torsion

Another consideration is the stress on flexures. For Silicon the maximum stress should not exceed about 1GPa (exact value depends on process, doping, etc.). The maximum stress,  $\tau_{max}$ , in a rectangular cross-section torsional flexure can be calculated using the following:<sup>10</sup>

$$\tau_{max} = \frac{3K_s Gb\theta_{mech}}{8L_f} \cdot \left[ 1 + 0.6095\left(\frac{b}{a}\right) + 0.8865\left(\frac{b}{a}\right)^2 - 1.8023\left(\frac{b}{a}\right)^3 + 0.91\left(\frac{b}{a}\right)^4 \right] \quad \text{for } a \geq b \quad (13)$$

Choice of the material affects the tolerable stress levels and frequency. The maximum scan angle can be determined by setting  $\theta_{max}$  equal to some fraction of the yield strength of the material. It should be noted that this stress is a function of scan angle and flexure dimensions, and not of operation frequency or mirror dimensions. Stress can be reduced by increasing  $L_f$  or by decreasing  $a$  and  $b$ . However, flexure dimensions can only be changed within a limited range. Long flexures lead to large package size. Using the analytical formulas presented so far makes it relatively easy task to explore the flexure design space for the desired characteristics.

## 5. ACTUATORS

The peak mechanical torque requirements of the scanner,  $T_{mech}$ , is given by:

$$T_{mech} = K_f \theta_{mech} / |H(\omega)| \quad (14)$$

where  $|H(\omega)|$  is the modulus of the scanner transfer function at the operation frequency of the scanner for the torsion mode. For resonant operation,  $|H(\omega_{res})|$  is equal to the mechanical  $Q$ -factor of the scanner. Resonant operation is attractive due to large gain in torque. Several actuation mechanisms are available for resonant scanners. Parallel plate electrostatic actuation is well known and discussed elsewhere. Main difficulty with parallel plate electrostatic actuation is the high-voltage requirements. Costly vacuum packaging is often required to increase  $Q$ -factor in order to lower actuation voltages. In this section, we'll briefly discuss out-of-plane comb-drive and a novel moving coil electromagnetic actuator that are both compact and efficient.

### 5.1. Comb Actuator

Basic comb scanner structure and comb fingers are illustrated in Figure 4. Comb-driven microscanners discussed here are developed by Fraunhofer IPMS, Germany.<sup>13</sup> Scan mirrors are Al coated and typically have 1-2mm diameter. Microfabrication is based on Single Crystalline SOI. The comb fingers have about 5  $\mu\text{m}$  width and 5 $\mu\text{m}$  gap in between, comb finger length is about 100  $\mu\text{m}$ . Trenches are formed across the die and filled with SiO<sub>2</sub> for electrical isolation of inner and outer gimbal frames and the fixed comb fingers. The actuator is attractive because it provides a compact 2D actuation where the actuator and the mechanical part are all integrated. Required voltages are about 20-25 Volts (in ambient air) to achieve sufficient  $\theta D$ -product and torsion frequency for barcode scanning or QVGA display applications.

Unlike the in-plane lateral mode, the torque produced by the torsional mode comb-actuators is strongly dependant on the tilt angle. The out-of-plane torque can be expressed as:

$$M(\theta) = 2N \frac{1}{2} \frac{dC}{d\theta} V(t)^2 \quad (15)$$

where  $N$  is the total number of comb fingers,  $C$  is the total capacitance,  $\theta$  is the tilt angle and  $V(t)$  is the periodic drive signal. The derivative of the total capacitance introduces the  $\theta$  dependence into the torque function. We have run simulations to model this derivative using MATLAB<sup>®</sup>. Fig. 4(c) shows the simulation results.

Figure 5 illustrates the basic frequency behavior of the scanner. The hysteresis in the response can be observed better in this figure. The path traced on the tilt-angle ( $\theta$ )—drive-frequency ( $f$ ) curve when frequency is increased quasi-statically from a lower frequency is different than the case, in which the frequency is swept down from a higher frequency. The interval between the two jump frequencies  $f_1$  and  $f_2$  is the *unstable region* of the response curve. Oscillations can start and stabilize only for frequencies above the second jump frequency, called *stability region*. Oscillations in the unstable region can only be observed if the excitation frequency is quasi-statically swept down to this region from the stable region above. At the critical frequencies, the jump in the oscillation amplitude is extremely abrupt.

Out-of plane mode comb actuators have time-varying spring stiffness, and this leads to a parametric oscillatory behavior, which exhibits interesting frequency response, transient response, and voltage controlled frequency behavior at particular subharmonic frequencies (illustrated in Figure 5(b)).

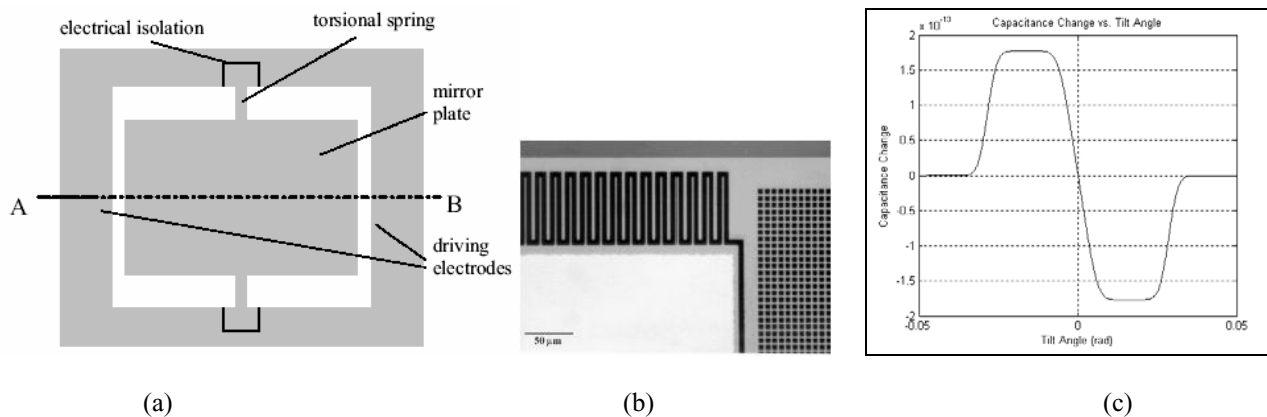


Figure 4: (a) Basic device structure; (b) comb-fingers for out-of-plane actuation; (c) Rate of change of total capacitance with respect to angular displacement. For small angles, a third order polynomial may be fitted to this curve.

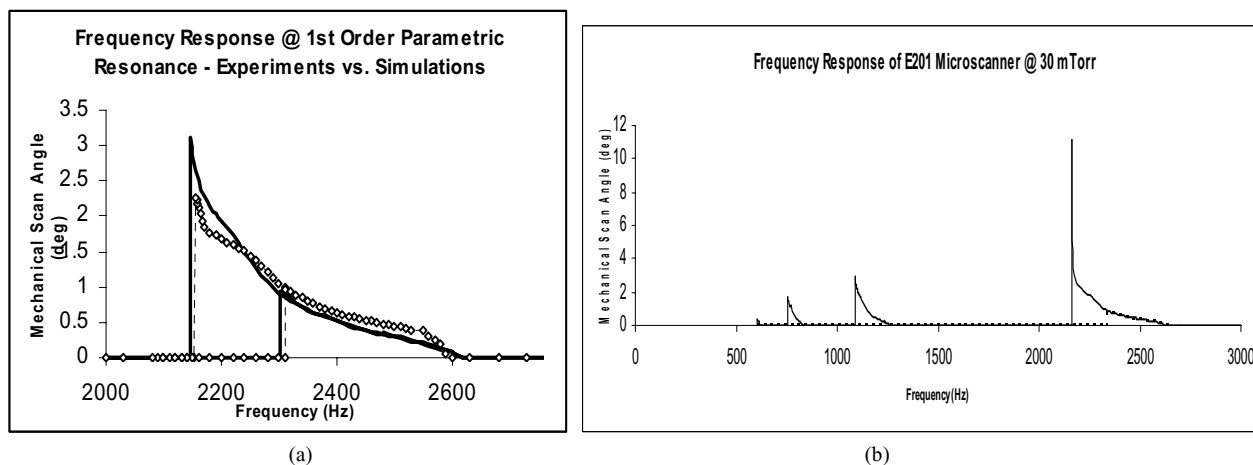


Figure 5: (a) Comparison of simulation (dashed line) and experimental (solid line) results for the 1st order parametric resonance in atmospheric pressure; (b) Experimental frequency response data at 30 mTorr illustrating multiple parametric resonances. Excitation signal is a square-rooted sine with 20 Vp-p for both plots

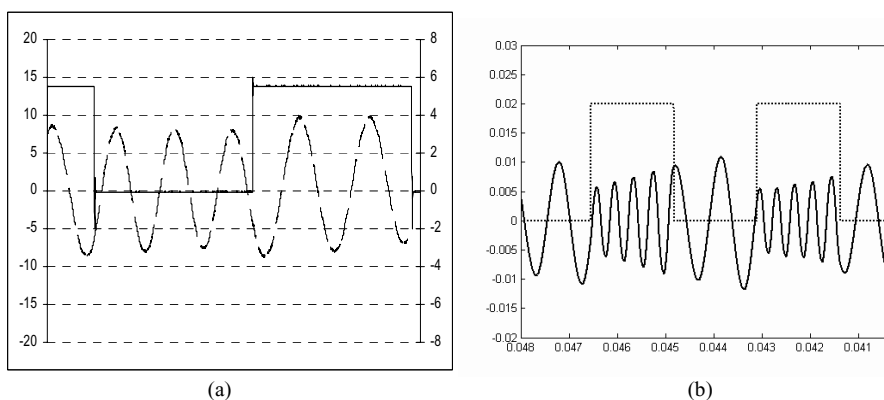


Figure 6: Alternating oscillation phenomenon at higher order resonances with 380 Hz square wave excitation. (a) Experimental result; (b) Simulation result

For square wave input, the response is not a pure sinusoid for high order resonances. Scan wave shows an unusual behavior and changes oscillation frequency and amplitude at each half cycle of the square wave. When excitation is in

the OFF state (meaning that no torque is present in the system), the system makes free oscillation at its natural resonant frequency, when the excitation is in the ON state, the mirror oscillates at a higher frequency, which can be calculated using the excitation and natural frequencies. This phenomenon is called *alternating oscillation frequency*. Fig. 6(a) shows the experimental results and Figure 6(b) shows our numerical simulation results illustrating the behavior. Such behavior is observed in higher order resonances.

### 5.2. Electromagnetic Actuator

Electromagnetic force is linear with current input to the electromagnetic coils in magnetic actuators. Therefore, arbitrary scan waveforms can be easily created. Two types of electromagnetic actuators can be envisioned. The first type is the moving coil actuator, where metal coils are deposited on the scanner and the scanner is placed in a static magnetic field generated by permanent magnets. The second type is the moving magnet actuator, where an array of magnets<sup>14</sup> or a layer of magnetic material (e.g. perm alloy)<sup>15</sup> is deposited on the scanner surface and an AC electromagnetic field is created using an electromagnet.

A moving coil electromagnetic actuator and the torsional scan mirror are depicted in Figure 7. There are external magnets around the scan frame where the drive coils are plated. The cross product of the magnetic field along the x-axis and the current along the y-axis produces a force along the z-axis. The opposite current direction on different sides of the coil generates forces in +z and -z directions, resulting in a net torque or twisting moment. The total magnetic torque generated by the actuator is the sum of the torque generated by each coil turn. The magnetic field,  $B$ , can be in the order of 0.3T to 0.7T or even larger in different magnet designs. The magnetic field strength increases with the magnet size and is limited by magnet saturation.<sup>16</sup>

The coils are planar and can cover the entire backside or a portion of the backside of the mirror. The coil current is inversely proportional to number of coil turns, while the dissipated power at the coil is independent of the number turns (assuming gap between coil turns is neglected). Thus, the number of turns can be determined based on driving circuit and micromachining considerations.

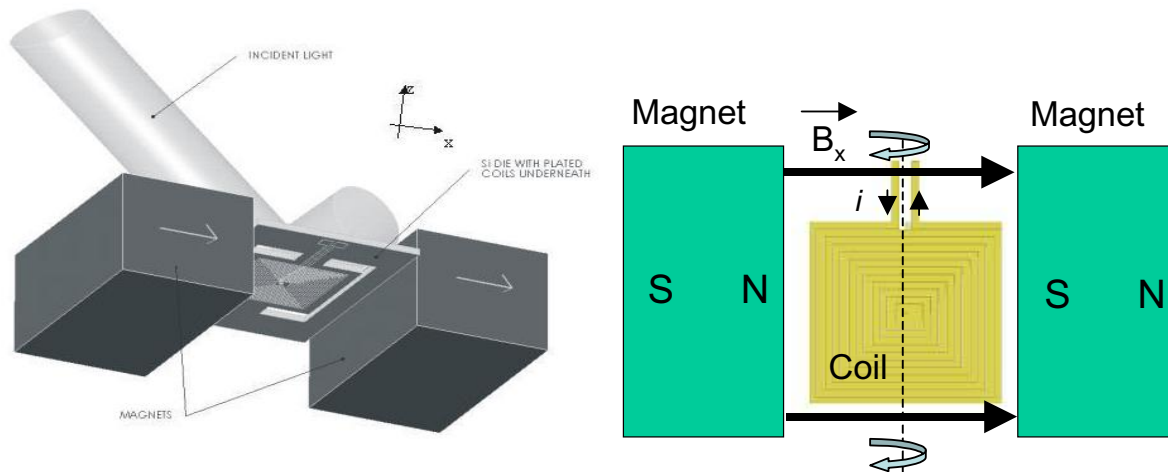


Figure 7: Torsional scanner, coils, and magnets for a moving-coil actuator scanner.

Coil density, resistivity, thermal properties, and fabrication process are important criteria in coil material selection. Gold and copper are commonly used as coil materials. Copper is preferred over gold due to its lower resistivity and lower weight. Thicker coils have lower resistance, however they add weight to the structure. One can deposit a single layer, stack multiple layers with an insulating layer in between, or deposit coils on both sides of the wafer. The power dissipated on the coils and the ambient temperature changes introduce a thermal load and can alter the flatness of the structure and the scan mirror. Coils on both sides increase the number of processing steps, but help athermalize the structure to maintain the mirror flatness. The coil thickness and layers need to be optimized based on the drive power, thermal, and weight requirements of the scanner.

### Novel Coil and Magnet Design:

In the above electromagnetic actuator, the sides of the coil in parallel with the B-field do not produce any torque. We designed a novel two-coil architecture and a novel magnet design that is placed underneath the coil, illustrated in Figure 8. The B-field direction illustrated in Figure 8(b) is perpendicular to the current direction on all four sides of each coil. Figure 8(c) shows the B-field perpendicular to each coil turn, producing larger torque. The new magnet design takes advantage of the fringing fields and the bottom magnets are substantially smaller than the side magnets used with single coil architecture. Compared to the first generation EM actuator design, the 2<sup>nd</sup> generation electromagnetic architecture has 6 times smaller volume and produces about twice the electromagnetic torque due to larger B-field from bottom magnets and due to utilization of the sides of the coils. The new coil and the magnet design provides a compact actuator design that doesn't change the scanner footprint area in the system. One difficulty with the new design is assembling 13 magnets, which requires a special fixture.

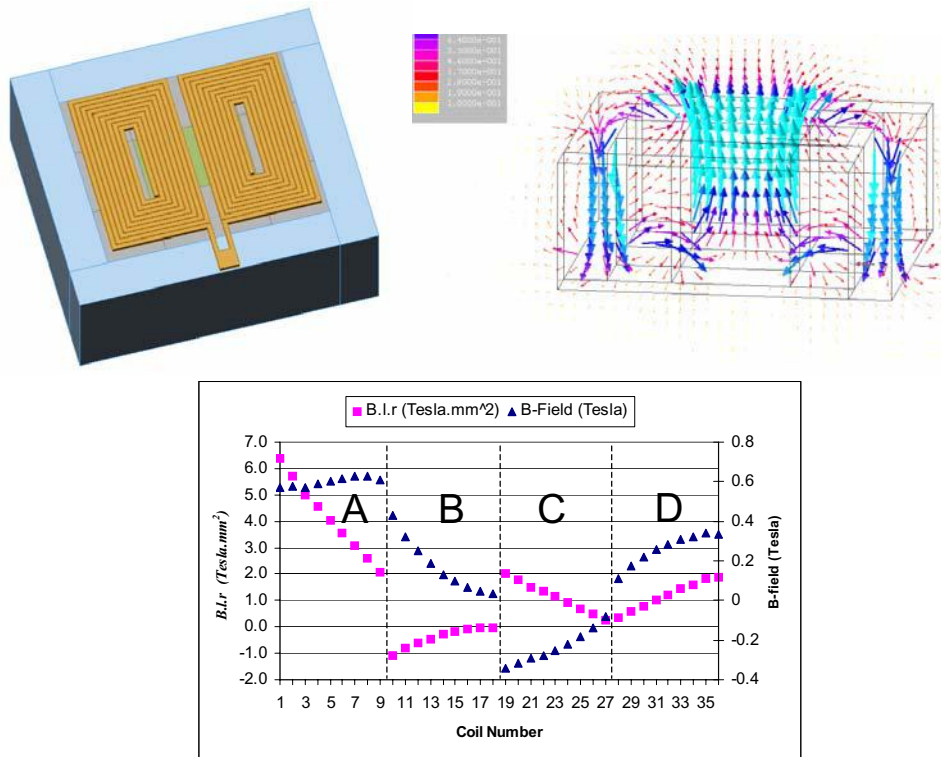


Figure 8 (a) Bottom view of the two-coil design, (b) magnetic field lines for the novel magnet design, (c) regions A, B, C, D show left, top, right, and bottom turns of one half of the coil in (a).

## 6. DISCUSSION AND CONCLUSIONS

Optical resolution and dynamic mirror flatness requirements define the scan mirror size and shape, and scan angle. Light sources also play an important role in deriving the scan mirror requirements. As a process technology, bulk micromachining of Silicon or SOI wafers should be preferred over surface micromachined scanners for high-resolution scanning systems. Torsional resonant scanner geometry discussed in this paper is able to meet the difficult requirements of dynamic displays as demonstrated by the SVGA-resolution NOMAD<sup>TM</sup> microdisplay system, developed by Microvision Inc, that use a biaxial MEMS scanner.

FEM simulations are generally time consuming when the design space is not well understood. The formulas in Tables 1 and 2 can be used to predict the mode frequencies, which give important information about the sequence of different modes and the relative frequency separation between modes. Once a good design point is reached using the analytical calculations, FEM simulations should be used for more accurate predictions using the exact mirror geometry. The formulas in the Tables include effects of Silicon material anisotropy and effective flexure beam inertia. An additional

correction factor is introduced based on the flexure width and flexure length ratios of the scanner, making the formulas valid even for flexure dimensions where Euler-Bernoulli beam theory becomes inaccurate.

High-performance scanners also demand low power, high-torque, and compact actuators. Out-of-plane comb actuators operate with low voltages, consume little power, and are compact. Many fundamental nonlinear characteristics of comb-driven microscanners are described. In linear scanners, one avoids having other resonances in the system close to the primary resonance of the scanner and its harmonics. For the nonlinear parametric resonance scanner, one should also pay attention to the subharmonic frequencies in the system.

Dual coil electromagnetic actuator can provide higher torque compared to comb actuators. Even though external magnets are required, in the two-coil design magnets are hidden underneath the scan mirror, reducing the system size substantially compared to side magnet EM actuators.

### ACKNOWLEDGMENTS

I'd like to thank Caglar Ataman, Cihan Kan, and Wyatt Davis for their help in different parts of this research.

### REFERENCES

- [1] H. Urey, Retinal Scanning Displays, in Encyclopedia of Optical Engineering, R. Driggers, Editor, Vol. 3, p. 2445-2457, Marcel Dekker, 2003.
- [2] H. Urey, "Diffractive Exit-Pupil Expander for Display Applications," Applied Optics, Vol. 40, No. 32, p.5840-5851, November 2001
- [3] H. Urey and K. D. Powell, "Microlens array-based exit pupil expander for full color display applications," in *Photon Management*, Proc. SPIE vol. 5456, Strasbourg, France, 2004.
- [4] Hakan Urey, "Spot size, depth of focus, and diffraction ring intensity formulas for truncated Gaussian beams," Applied Optics, Vol. 43, No. 3, Jan 2004
- [5] M. Freeman, "Miniature high-fidelity displays using a biaxial MEMS scanning mirror," in MOEMS Display and Imaging Systems,
- [6] Hakan Urey, David Wine, and Thor Osborn, "Optical performance requirements for MEMS-scanner based microdisplays," Conf. on MOEMS and Miniaturized Systems, SPIE Vol. 4178, Santa Clara, California, 2000, pp. 176-185.
- [7] H. Urey, D. W. Wine, and J. R. Lewis, "Scanner design and resolution tradeoffs for miniature scanning displays," in *Flat Panel Display Technology and Display Metrology*, Proc. SPIE vol. 3636, pp. 60-68, San Jose, California, 1999
- [8] A. Garnier, T. Bourouina, E. Orsier, T. Masuzawa, H. Fujita, T. Hiramoto, and J.-C. Peuzin, "A fast simple and robust 2-D micro-optical scanner based on contactless magnetostrictive actuation," in Proc. MEMS'2000, Miyazaki, Japan, 2000, pp. 715-720.
- [9] W. Weaver, Jr., S.P. Timoshenko, D.H. Young, Vibration problems in engineering, Wiley, New York, 1990
- [10] W. C. Young and R. G. Budynas, *Roark's Formulas for Stress and Strain*, McGraw-Hill, New York, 7th Edition, 2002
- [11] W. O. Davis, Oliver M. O'Reilly, and A. P. Pisano, "On the Nonlinear Dynamics of Tether Suspensions for MEMS," to appear in *Journal of Vibration and Acoustics*, v. 126, July 2004.
- [12] T. N. Juneau, *Micromachined Dual Input Axis Rate Gyroscope*, Ph.D. thesis, U. C. Berkeley, 1998.
- [13] H. Schenk, P. Dürr, D. Kunze, H. Lakner, H. Kück, "A resonantly excited 2D micro-scanning-mirror with large deflection," *Sensors and Actuators A*, Vol. 89, p.104-111, 2001
- [14] T. M. Liakopoulos, W. Zhang, and C. H. Ahn, "Micromachined Thick Permanent Magnet Arrays on Silicon Wafers", *IEEE Trans. on Magnetics*, Vol. 32, No. 5, p.5154-5156, 1996.
- [15] C. Liu, "Development of surface micromachined magnetic actuators using electroplated permalloy," *Mechatronics*, Vol. 8, No. 5, p.613-633, 1998.
- [16] H. Urey, F. DeWitt, K. Powell, and M. Bayer, "High-Frequency Raster Pinch Correction Scanner for Retinal Scanning Displays," *MOEMS and Miniaturized Systems*, SPIE Vol. 4561, San Francisco, California, October 2001.